CoFe2O4 Nanomaterials: Effect of Annealing Temperature on Characterization, Magnetic, Photocatalytic, and Photo-Fenton Properties

Authors:

Nguyen Thi To Loan, Nguyen Thi Hien Lan, Nguyen Thi Thuy Hang, Nguyen Quang Hai, Duong Thi Tu Anh, Vu Thi Hau, Lam Van Tan, Thuan Van Tran

Abstract:

In this research, structural, magnetic properties and photocatalytic activity of cobalt ferrite spinel (CoFe2O4) nanoparticles were studied. The samples were characterized by X-ray powder diffraction (XRD), energy dispersive X-ray (EDX), scanning electron microscopy (SEM), transmission electronic microscopy (TEM), Brunauer?Emmett?Teller (BET), Fourier transform infrared spectroscopy (FTIR), and UV-visible diffused reflectance spectroscopy (DRS) analysis. The XRD analysis revealed the formation of the single-phase CoFe2O4 with a cubic structure that is annealed at 500?700 °C in 3 h. The optical band gap energy for CoFe2O4 was determined to be in the range of 1.57?2.03 eV. The effect on the magnetic properties of cobalt ferrites was analyzed by using a vibrating sample magnetometer (VSM). The particle size and the saturation magnetization of cobalt ferrite nanoparticles increased with increasing annealing temperature. The photocatalytic activity of CoFe2O4 nanoparticles was investigated by using rhodamine B dye under visible light. The decomposition of rhodamine B reached 90.6% after 270 min lighting with the presence of H2O2 and CF500 sample.

CoFe₂O₄ Nanomaterials: Effect of Annealing Temperature on Characterization, Magnetic, Photocatalytic, and Photo-Fenton Properties

Nguyen Thi To Loan [1,*] **, Nguyen Thi Hien Lan** [1] **, Nguyen Thi Thuy Hang** [2] **, Nguyen Quang Hai** [3] **, Duong Thi Tu Anh** [1] **, Vu Thi Hau** [1] **, Lam Van Tan** [4,5] **and Thuan Van Tran** [4,6,*]

[1] Faculty of Chemistry, Thai Nguyen University of Education, Thai Nguyen City 24000, Vietnam; nguyenhienlan@dhsptn.edu.vn (N.T.H.L.); duongtuanh@dhsptn.edu.vn (D.T.T.A.); vuthihau-khoahoa@dhsptn.edu.vn (V.T.H.)
[2] Thai Nguyen University of Technology, Thai Nguyen City 24000, Vietnam; thuyhangdhktcn@gmail.com
[3] Faculty of Physics, Thai Nguyen University of Education, Thai Nguyen City 24000, Vietnam; nguyenquanghai@dhsptn.edu.vn
[4] NTT Hi-Tech Institute, Nguyen Tat Thanh University, Ho Chi Minh City 700000, Vietnam; lamvantan101076@gmail.com
[5] Ben Tre's Department of Science and Technology, Ben Tre Province 86000, Vietnam
[6] Center of Excellence for Green Energy and Environmental Nanomaterials, Nguyen Tat Thanh University, Ho Chi Minh City 700000, Vietnam
* Correspondence: nguyentoloan@dhsptn.edu.vn (N.T.T.L.); tvthuan@ntt.edu.vn (T.V.T.)

check for updates

Abstract: In this research, structural, magnetic properties and photocatalytic activity of cobalt ferrite spinel (CoFe₂O₄) nanoparticles were studied. The samples were characterized by X-ray powder diffraction (XRD), energy dispersive X-ray (EDX), scanning electron microscopy (SEM), transmission electronic microscopy (TEM), Brunauer–Emmett–Teller (BET), Fourier transform infrared spectroscopy (FTIR), and UV-visible diffused reflectance spectroscopy (DRS) analysis. The XRD analysis revealed the formation of the single-phase CoFe₂O₄ with a cubic structure that is annealed at 500–700 °C in 3 h. The optical band gap energy for CoFe₂O₄ was determined to be in the range of 1.57–2.03 eV. The effect on the magnetic properties of cobalt ferrites was analyzed by using a vibrating sample magnetometer (VSM). The particle size and the saturation magnetization of cobalt ferrite nanoparticles increased with increasing annealing temperature. The photocatalytic activity of CoFe₂O₄ nanoparticles was investigated by using rhodamine B dye under visible light. The decomposition of rhodamine B reached 90.6% after 270 min lighting with the presence of H₂O₂ and CF500 sample.

Keywords: cobalt ferrite; magnetic properties; solution combustion method; rhodamine B; photocatalytic activity

1. Introduction

Among many ferrites, cobalt ferrite magnetic nanoparticles are attracting much attention because of their high coercivity, magnetocrystalline anisotropy, moderate saturation magnetization, chemical stability, wear resistance, electrical insulation, and structure [1]. Structurally, in the inverse spinel of the ferrite, tetrahedral sites are generally occupied by Fe^{3+} ions, whereas octahedral sites (B-sites) are inhabited by Co^{2+} and Fe^{3+} ions [2]. To alter structure and magnetic properties of ferrite nanoparticles, it is necessary to modify their composition and microstructures via different preparation routes [2]. CoFe₂O₄ nanoparticles were previously prepared by a wide array of synthesis routines, such as

sol-gel [3,4], hydrothermal method [5], chemical co-precipitation [6,7], solvothermal [8], solid-state method [9], and solution combustion [10–13]. For each synthesis method, it was found that the annealed temperature played a key role in determining the structure and properties of the obtained product. In recent years, photocatalytic oxidation of various dyes using ferrites has drawn a great deal of attention, opening new trends in the environmental remediation [14–16].

Currently, contamination of the water environment has been alarming due to the widespread use of organic compounds in manufacturing processes and the rapid development of dyeing industries. These dye compounds existing in water pose a direct threat to public health and to animal and aquatic life due to their toxicity, endocrine-disrupting capability, and mutagenic or potentially carcinogenic properties [17]. One of the most effective methods of solving this problem is advanced oxidation processes (AOPs). Among different AOPs, the photo-Fenton-like reaction was widely studied because it can produce more oxidative species such as hydroxyl radicals ($^\bullet$OH) to accelerate the reaction [18]. This method is based on the use of semiconductors and oxidant and light sources to perform the decomposition of organic matter. The advantages of the photo-Fenton processes consist of environmental friendliness and the ability to decompose completely organic pollutants into non-toxic inorganic substances, these being CO_2 and H_2O. Spinel ferrite materials have received wide application as photocatalysts due to their structural composition and thermal and chemical stability toward various reaction conditions [18]. The photo-Fenton reagent using ferrite can be easily recovered from the solution by an external magnetic field and is available for reutilization.

Abul Kalam et al. reported the photocatalytic activity of cobalt ferrite magnetic nanoparticles for degradation of methylene blue with H_2O_2 under visible light irradiation, and achieved very good performance [15]. P. Annie Vinosha et al. synthesized $NiFe_2O_4$ by co-precipitation technique. The photocatalytic application for the synthesized sample was studied for the degradation of methylene blue dye. In the presence of H_2O_2 and ferrites, methylene blue degradation efficiency reached ~30% in the dark but degradation improved to ~99% in the irradiation light [19]. $MgFe_2O_4$ nanoparticles synthesized by a solution combustion method exhibited a high ability for Photo-Fenton-like degradation of methylene blue [20]. In the photo-Fenton processes, hydrogen peroxide is used commonly as an oxidant. Hydrogen peroxide is safe and easy to handle and poses no lasting environmental threat because it readily decomposes to water and oxygen [17].

One of the major pollutants discharged from various industries is dyes [21–23]. Previous reports have revealed that thousands of new dyes have been synthesized and commercialized, with the total amount of approximately one million tons being consumed throughout the world [24,25]. Ever-increasing utilization and direct discharge without treatment of colored effluents have been considered as a problematic obstacle, affecting the photosynthesis of aquatic lives because of the reduction of the ability of light penetration [26]. Amid the most emergent synthetic dyes, rhodamine B (RhB) is a virtually hazardous and non-biodegradable dye [27]. In chemical essence, this compound is categorized as a cationic and soluble dye, in accordance with the existence of highly stable tertiary amine and carboxylic groups in its molecular structure. It is thus found to have a profound impact on living creatures as well as ambient environment via a range of approaches on direct or indirect exposure [28]. With such harmful and dangerous properties to many organisms, effective removal of dyes from wastewater is essential, but currently remains a challenge [29].

To eliminate the RhB contamination in wastewater, the adoption manifold feasible methods has been suggested, involving adsorption [30], electro-Fenton process [31], and microfiltration membrane [32]. For instance, Tawfik et al. synthesized the nano-sized polyamide-grafted carbon microspheres via interfacial polymerization, exhibiting a promising adsorption performance towards RhB at 19.9 mg/g [33]. Recently, Mustafa et al. have successfully attained a kind of eco-friendly activated carbon-based modified nanocomposite that combined carbon with bimetallic Fe and Ce nanoparticles [34]. Regardless of giving promising results in high surface area (~423 $m^2 \cdot g^{-1}$) and adsorption capacity (324.6 $m^2 \cdot g^{-1}$) towards RhB, the complicated preparation procedure limits applications of the synthesized nanocomposite. On the other hand, although the introduction of

minerals as adsorbents for treating RhB have been developed, such approaches seem to confront many obstacles relating to material stability, recyclability, fabrication cost, and the reliance on post-treatment separation [35–37]. With high stability, magnetism, and photocatalysis, $CoFe_2O_4$ nanoparticles are expected to deal with RhB pollution in water efficiently.

In this present report, the spinel cobalt ferrites nanoparticles are characterized for their structural, morphological, optical, and magnetic properties using various methods. In addition, the photocatalytic activity of samples was investigated by the degradation process of rhodamine B.

2. Materials and Methods

2.1. Materials

Cobalt nitrate hexahydrate ($Co(NO_3)_2 \cdot 6H_2O$), iron nitrate nonahydrate ($Fe(NO_3)_3 \cdot 9H_2O$), urea (CH_4N_2O), rhodamine B ($C_{28}H_{31}ClN_2O_3$), and hydrogen peroxide were obtained from Merck and used as received, without further purification.

2.2. Synthesis of CoFe₂O₄ Nanoparticles

The synthesis of cobalt ferrite was performed via solution combustion method using urea as fuel [11]. The process commenced with the dissolution of urea in the water, followed by the addition of $Co(NO_3)_2 \cdot 6H_2O$ and $Fe(NO_3)_3 \cdot 9H_2O$ at an appropriate amount and mole ratio under vigorous stirring. The resultant mixed solution was stirred further to afford a gel, which was then subjected to heating at 70 °C for 12 h in an oven. The obtained powder product was calcined at four different temperatures ranging from 500 to 800 °C for 3 h with a heat rate of 5 °C min⁻¹, and the subsequent products were labeled as CF500, CF600, CF700, and CF800 respectively.

2.3. Characterizations

The first characterization involved determining the crystallite size, r, of spinel using Scherrer's formula as follows:

$$r = \frac{k\lambda}{\beta \cos\theta} \tag{1}$$

where λ, k, β, and θ are the X-ray wavelength, Scherrer's constant ($k = 0.89$), the full width at half maximum observed in radians, and the angle of diffraction of the (311) peak with the highest intensity, respectively. θ and β were obtained via X-ray diffraction (XRD) results using a D8 Advance diffractometer (Brucker, Madison, WI, USA) instrument with CuK_α radiation ($\lambda = 1.5406$ Å) in a 2θ angle ranging from 20 to 70° with a step of 0.03°.

The second characterization regarding morphology of the particles was obtained via scanning electron microscope (SEM, Hitachi S-4800, Tokyo, Japan) and transmission electron microscopy (TEM, JEOL-JEM-1010, Tokyo, Japan). The composition of the samples was analyzed by energy dispersive X-ray spectroscopy (EDX, JEOL JED 2300 Analysis Station, Tokyo, Japan). N_2-sorption investigation was performed to obtain the Bet-specific surface area of the product. A surface analyzer instrument (a Quantachrome Nova 2200, Boynton Beach, FL, USA) was employed to obtain the isotherm at 77 K. The specific surface area was calculated via the Brunauer–Emmet–Teller (BET) method. The spinel structure was affirmed by Fourier transform infrared spectroscopy (FTIR Affinity-1S, Shimadzu, Tokyo, Japan). A UV-VIS absorption spectrometer (U-4100, Hitachi, Japan) was employed to obtain the optical absorption spectra. To elaborate magnetic properties of samples, a vibrating sample magnetometer (VSM, Ha Noi, Vietnam) operating at room temperature was utilized.

2.4. Photocatalytic Degradation of Rhodamine B

Multiple ferrite samples synthesized at different annealing temperatures were examined for photodegradation performance against Rhodamine B (RhB) aqueous solution. The irradiation source was 30 W LED lamps (Philips). The experiment commenced with the addition of 100 mg of ferrite

sample into 100 mL of 10 mg. L^{-1} RhB aqueous solution. Following that, stirring was carried out in the dark for 30 min to allow the solution to reach the adsorption–desorption equilibrium state, followed by the addition of 1.5 mL of 30% H_2O_2. Consequently, visible light irradiation started and the reaction took place under stirring. After specific periods, 5 mL of aliquots were removed and subjected to centrifugation for particle separation. RhB concentration was determined using an ultraviolet-visible spectrophotometer (UV-1700 Shimadzu, Tokyo, Japan) at 553 nm. The degradation efficiency of the ferrite against RhB (H) was calculated as follows:

$$H = \frac{C_o - C_t}{C_o} \times 100\% \tag{2}$$

where C is the concentration of RhB. The subscript 0 and t denote equilibrium state and time (t) after irradiation, respectively.

3. Results and Discussion

3.1. Structural Analysis

Different XRD patterns of cobalt ferrites corresponding to different annealing temperatures are shown in Figure 1. The reflection peaks corresponded to the characteristic spacing between (220), (311), (400), (511), and (440) plans of a cubic spinel structure, providing clear evidence of the formation of cobalt ferrite (JCPDS number 22–1086) [5]. α-Fe_2O_3 peaks corresponding to secondary impurities were observed for the sample annealed at 800 °C, which was possibly caused by sample decomposition [38]. Table 1 lists the average crystallite size (r), calculated using (1), and the lattice parameter (a), obtained using the formula $a^2 = d^2/(h^2 + k^2 + l^2)$ with inputs obtained from X-ray diffraction data. The mean crystallite size ranged from 9 to 29 nm and increased with elevated annealing temperature [29]. The lattice parameter for the samples of cobalt ferrites nanoparticles varied from 8.3347 to 8.3745 Å.
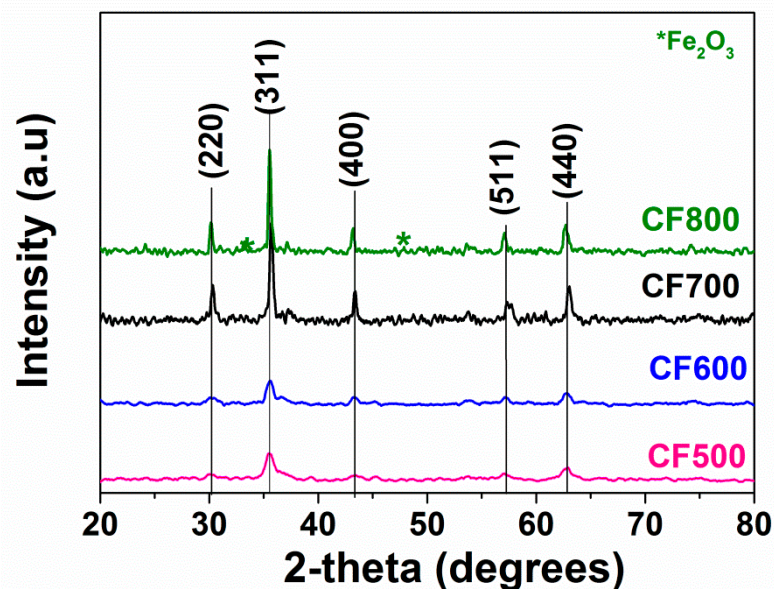

Figure 1. X-ray diffractions of $CoFe_2O_4$ nanoparticles annealed at 500–800 °C.

Table 1. Average crystallite size (r), lattice parameter (a), unit cell volume (V), wave number (ν_1 and ν_2) for the tetrahedral and octahedral site, respectively, and Brunauer–Emmet–Teller (BET) surface area of all the $CoFe_2O_4$ samples.

Samples	r (nm)	a (Å)	V (Å^3)	ν_1 (cm^{-1})	ν_2 (cm^{-1})	S_{BET} (m$^2 \cdot$g^{-1})
CF500	9	8.37	587.32	526	411	12.69
CF600	11	8.36	584.53	530	409	7.55
CF700	23	8.33	578.98	532	408	3.94
CF800	29	8.36	585.23	522	412	1.58

FTIR spectra of $CoFe_2O_4$ nanoparticles annealed at different temperatures are displayed in Figure 2. The cobalt ferrite samples exhibited two vibration bands at wave number 522–532 cm^{-1} (ν_1) and at 408–412 cm^{-1} (ν_2), corresponding to the stretching vibration of the M-O bond in tetrahedral and octahedral sites (Table 1). A. Kalam et al. [15] observed that the vibration mode between tetrahedral metal ion and oxygen complex gives rise to the high-frequency band in the range of 597–615 cm^{-1}, whereas stretching vibration between octahedral metal ion and oxygen complex gives rise to the weak frequency band in the range of 412–400 cm^{-1} in the case of cobalt ferrite, which is an inverse spinel ferrite.

The FTIR results confirmed that the samples had a spinel structure of $CoFe_2O_4$, which was revealed by the XRD results.
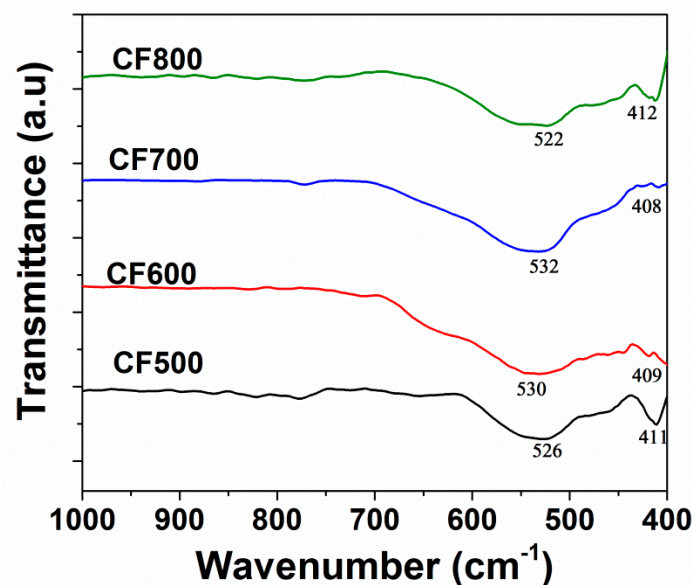
Figure 2. Fourier transform infrared (FTIR) spectrum of CF500–CF800 samples.

Figure 3 shows the SEM micrographs of $CoFe_2O_4$ nanoparticles annealed at different temperatures. The SEM images indicated that particles were agglomerated and spherical. In addition, the crystalline size of the samples seemed to increase proportionally with annealing temperature, which was consistent with the results of XRD analysis. The agglomeration could be explained by the interaction between magnetic particles that occurred during annealing under high temperatures. In addition, it was previously found that higher annealing temperature inevitably causes moderate agglomeration [2].
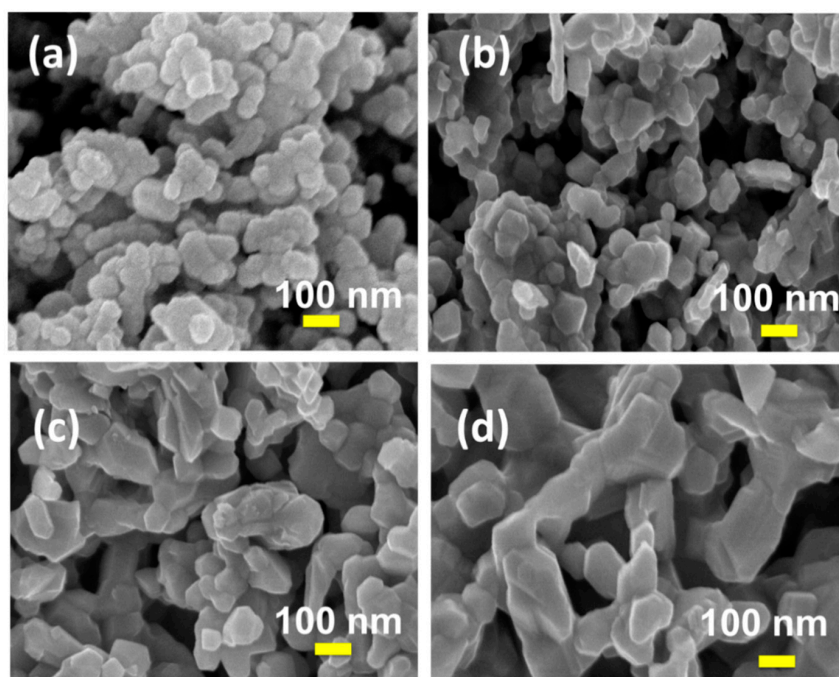
Figure 3. Scanning electron microscopy (SEM) of CoFe$_2$O$_4$ nanoparticles: (**a**) CF500, (**b**) CF600, (**c**) CF700, (**d**) CF800.

TEM images (Figure 4a) of the CoFe$_2$O$_4$ annealed at 500 °C revealed that the particle size was approximately 20 nm. Compositional determination was performed by energy dispersive X-ray spectroscopy (EDX) analysis, showing peaks corresponding to Co, Fe, and O elements of the CF500 sample (Figure 4b).

Element	Weight%	Atomic%
O K	29.64	59.92
Fe K	48.37	28.01
Co K	21.99	12.07
Totals	100.00	
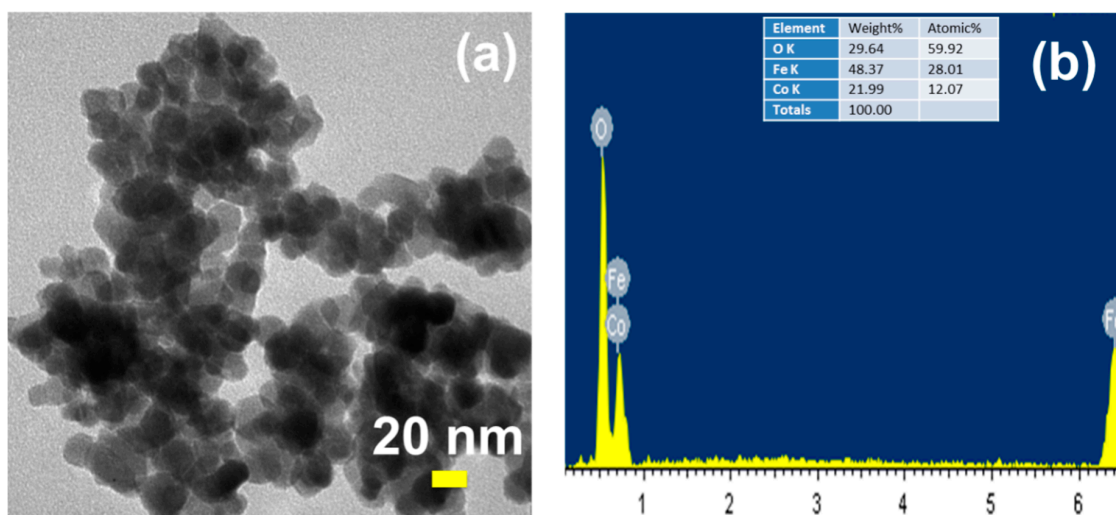
Figure 4. Transmission electronic microscopy (TEM) (**a**) and energy dispersive X-ray (EDX) (**b**) of the CF500 sample.

Isotherm of N$_2$ adsorption–desorption of products annealed at 500–800 °C are displayed in Figure 5. The decrease in the cobalt ferrites surface area was observed with the increase in annealing temperature (Table 1). The CoFe$_2$O$_4$ nanoparticles synthesized at 500 °C achieved the highest specific surface area of 12.69 m^2·g^{-1}.

Thus, annealing temperature affected the particle size, morphology, and surface area of cobalt ferrites.
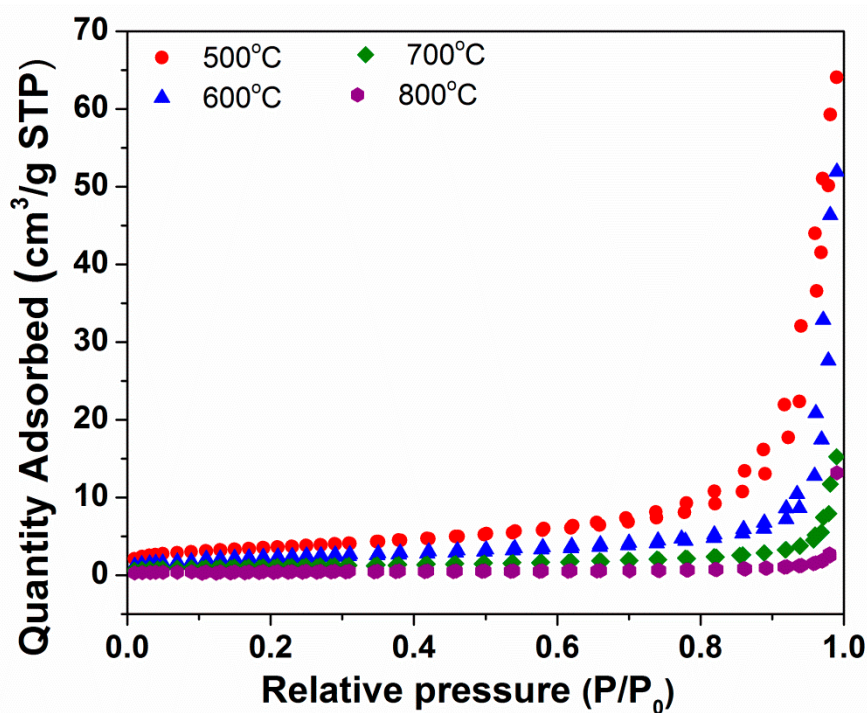
Figure 5. N_2 adsorption–desorption isotherm of CF500, CF600, CF700, and CF800.

Kubelka–Munk model was employed to calculate the band gaps (E_g) of $CoFe_2O_4$ nanoparticles using the absorption coefficient (α) calculated from diffuse reflectance spectra (DRS), as follows [39,40]:

$$F(R) = \alpha = \frac{(1-R)^2}{2R} \tag{3}$$

where F(R) is the Kubelka–Munk function, α is the absorption coefficient, and R is the reflectance. The band gap energy (E_g) of $CoFe_2O_4$ nanoparticles can be calculated by the following equation:

$$\alpha h\nu = A(h\nu - E_g)^n \tag{4}$$

where $h\nu$, α, A, and n represent energy of the photon, the absorption coefficient, the material parameter, and the transition parameter, respectively. n = 2 represents indirect transitions [41]. To determine the optical band gap energy (E_g), $(\alpha h\nu)^2$ was plotted against photon energy ($h\nu$) to produce multiple Wood–Tauc plots (Figure 6). The band gap values of CF500, CF600, CF700, and CF800 samples were found to be 1.57, 1.66, 1.90, and 2.03 eV, respectively. This indicated that the annealing affected the optical band gap energy of $CoFe_2O_4$ nanoparticles. The optical band gap energy value increased with increasing temperature in annealed samples.
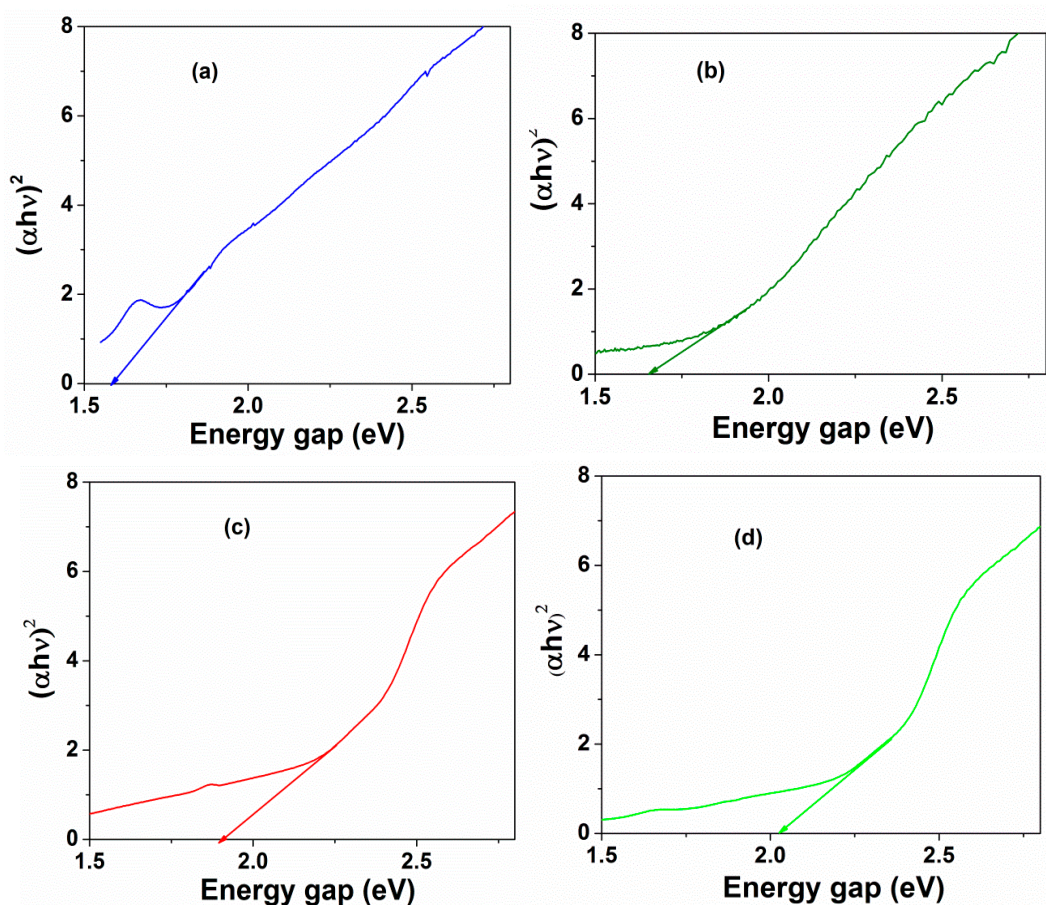
Figure 6. Wood–Tauc plots for CoFe$_2$O$_4$ nanoparticles: (**a**) CF500, (**b**) CF600, (**c**) CF700, (**d**) CF800.

3.2. Magnetic Properties

The magnetic properties of ferrites could be largely determined by various elements such as density, grain size, anisotropy, and A–B exchange interactions [1]. In this investigation, obtained ferrite products annealed at different temperatures were subjected to M–H hysteresis measurements carried out at room temperature. Various magnetic properties including saturation magnetization (M$_s$), coercivity (H$_c$), and remanent magnetization (M$_r$) are listed in Figure 7 and Table 2. It was observed that M$_s$ value showed a positive correlation with particle size. This was in line with Kumar et al., suggesting that increased particle size could lead to improved magnetization [2].

Table 2. Magnetic parameter of the CoFe$_2$O$_4$ nanoparticles.

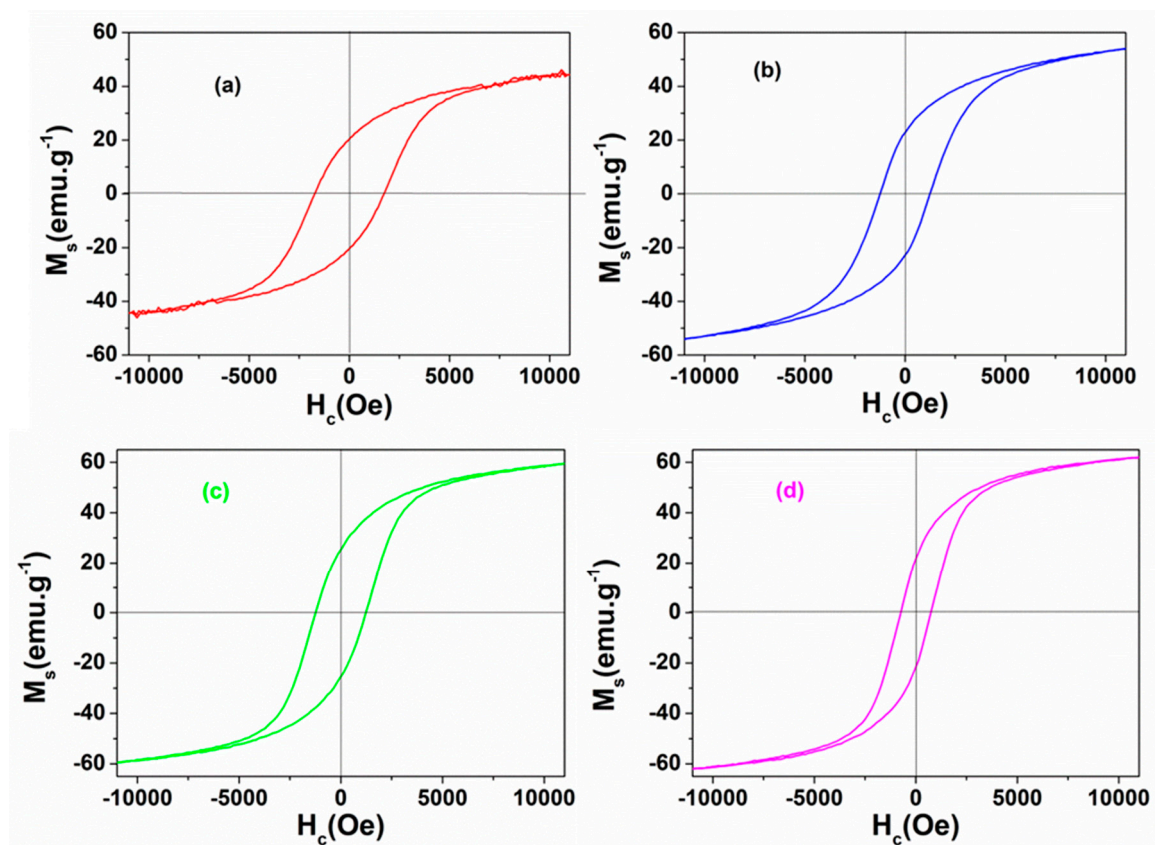| Samples	M$_s$ (emu/g)	H$_c$ (Oe)	M$_r$ (emu/g)
CF500	44.41	1739.45	20.36
CF600	53.86	1234.10	22.88
CF700	59.40	1234.20	27.89
CF800	61.80	762.04	27.83

Figure 7. Hysteresis loop of CoFe$_2$O$_4$ nanoparticles: (**a** CF500, (**b**) CF600, (**c**) CF700, (**d**) CF800.

3.3. Photochemical Activities

Figure 8 represented the photocatalytic degradation of RhB versus irradiation time in different conditions. Generally, absorption peaks observed at 501 and 553 nm could be attributable to the absorption fully de-ethylated and tetraethylated rhodamine B molecules, respectively [41]. The role of oxidant and catalyst was further elaborated by performing reactions under typical conditions that were neither H$_2$O$_2$ nor CoFe$_2$O$_4$. Firstly, RhB degradation efficiency reached a marginal percentage, at just 10.2%, under visible light after 270 min in the sole presence of H$_2$O$_2$. This implied that RhB dye could be hardly photodegraded in the absence of CoFe$_2$O$_4$ catalyst. In the presence of CoFe$_2$O$_4$ sample without oxidation reagent H$_2$O$_2$, RhB degradation efficiency achieved 9.4% (in the dark) and 32.5% (under light irradiation) after 270 min. In the absence of light, 21.3% of RhB was degraded while using both CoFe$_2$O$_4$ and H$_2$O$_2$. Abul et al. also observed similar results by using CoFe$_2$O$_4$ as a catalyst for the degradation of methylene blue in liquid under air atmosphere [15].

Grasping this improvement, we speculated about an even better photodegradation efficiency when CoFe$_2$O$_4$ and H$_2$O$_2$ were combined for the next photoreaction. Photocatalyzed degradation efficiency (%) towards RhB under visible light irradiation and in the presence of CoFe$_2$O$_4$ and H$_2$O$_2$ against the interval irradiation time is indicated in the UV-visible spectra in Figure 9. Indeed, all the samples of CoFe$_2$O$_4$ (CF) nanoparticles offered an enhancement in catalytic performance, but the percentages of RhB decomposition varied according to the distinct annealing temperature (500, 600, 700, and 800 °C). The photocatalytic degradation efficiency of RhB was evaluated at about 90.6%, 67.6%, 51.6%, and 42.8% after 270 min of lighting in the presence of H$_2$O$_2$ and CF500, CF600, CF700, and CF800, respectively.
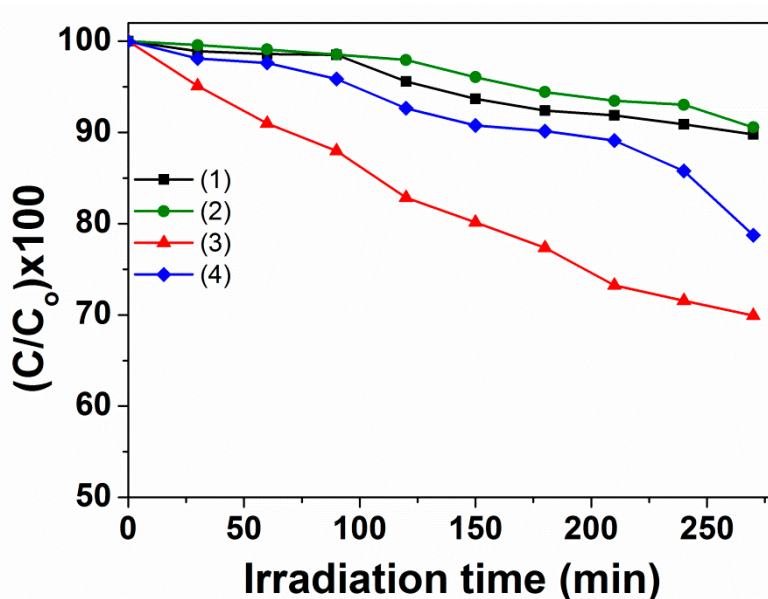
Figure 8. The plots of $(C/C_o) \times 100$ versus irradiation time (t) in different conditions: (**1**) H_2O_2, (**2**) CF500 + dark, (**3**) CF500 + light, (**4**) CF500 + H_2O_2 + dark.
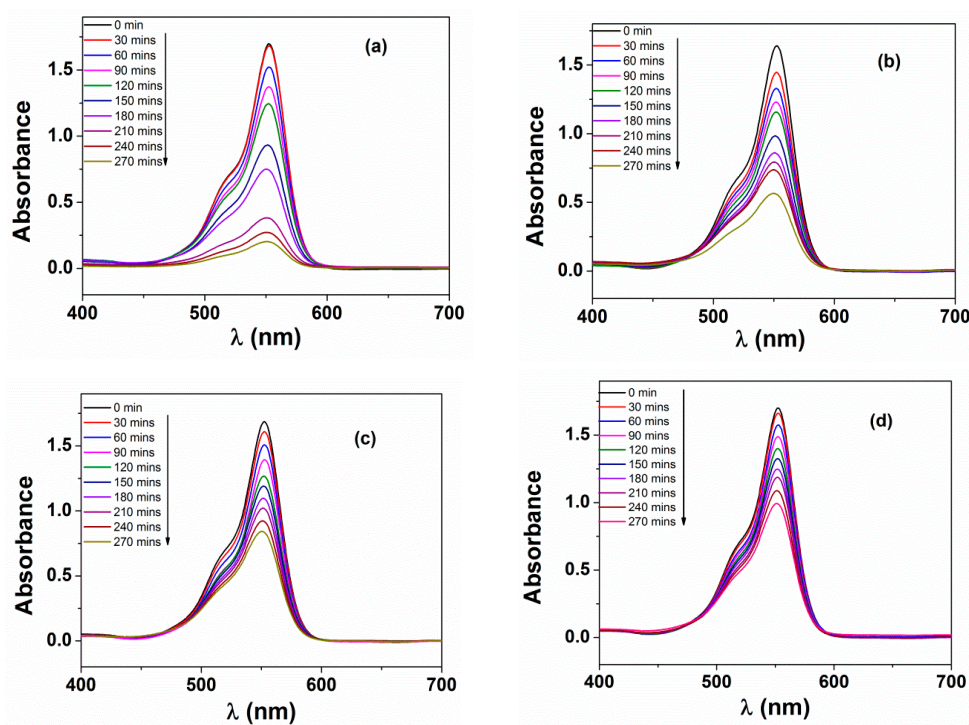
Figure 9. UV-visible spectra of RhB degraded by (**a**) H_2O_2 + CF500, (**b**) H_2O_2 + CF600, (**c**) H_2O_2 + CF700, (**d**) H_2O_2 + CF800 after 270 min of lighting.

The pollutant degradation rate could be substantially increased due to highly oxidative hydroxyl ($^{\bullet}$OH) radicals created by the heterogeneous photo-Fenton process, in the presence of spinel ferrite as a heterogeneous catalyst, using H_2O_2 as oxidant under light irradiation [15,42]. The mechanism of the heterogeneous photo-Fenton reaction was shown according to the following equations:

$$Fe^{3+} + H_2O_2 + h\nu \rightarrow Fe^{2+} + HOO^{\bullet} + H^+$$

$$Fe^{2+} + H_2O_2 + h\nu \rightarrow Fe^{3+} + {}^{\bullet}OH + OH^-$$
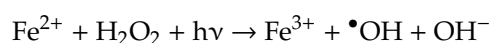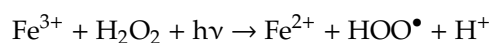
where Fe^{3+} and Fe^{2+} represent the iron species on the surface of a heterogeneous catalyst.

Due to Fe(II, III) cycling, the stability of the ferrite system is maintained during the degradation process and the active species are generated continuously [15].

The peak photocatalytic degradation efficiency for CF500 (90.6%) was due to the effective crystallite size (9 nm), separation, and prevention of electron-hole pair (e^-/h^+) recombination [43]. Photocatalytic performance of CF500 with the largest degradation rate could be interpreted via plausible hypotheses based on the following foundations:

(i)   It was found that CF500 possessed the lowest pore sizes, which is indicative of a high surface area of nanoparticles. This could accelerate the adsorption of RhB molecules on the surface, leading to a higher likelihood of $^{\bullet}OH$ radical formation [43].

(ii)   More importantly, CF500 nanoparticles with the lowest bandgap (1.57 eV) were more likely to form the electron–hole pair under visible light irradiation, dominating the charge carriers with oxidation of RhB [15].

(iii) Samples that were calcined at a higher temperature had greater band gap values, which possibly deferred the electron–hole pair recombination induced by visible light irradiation [44].

Figure 10 depicted the plots with different pseudo first order rates, which were obtained by fitting the following equation:

$$\ln\left(\frac{C_o}{C_t}\right) = kt$$

where C is the RhB concentration. The subscripts 0 and t denote initial state and time t after irradiation. k is the pseudo first order rate kinetics.

With the higher the coefficient of determination ($R^2 > 0.9$), the proposed model was highly compatible [45,46]. The estimated parameters, including pseudo first order rate constant k values and R^2 values, are shown in Table 3. The first order rate constant for CF500 was 0.839×10^{-2} min^{-1}, and it was 3.9 times faster than that of CF800. High R^2 values also confirmed the adherence of the photocatalytic degradation of RhB to the first order kinetics.
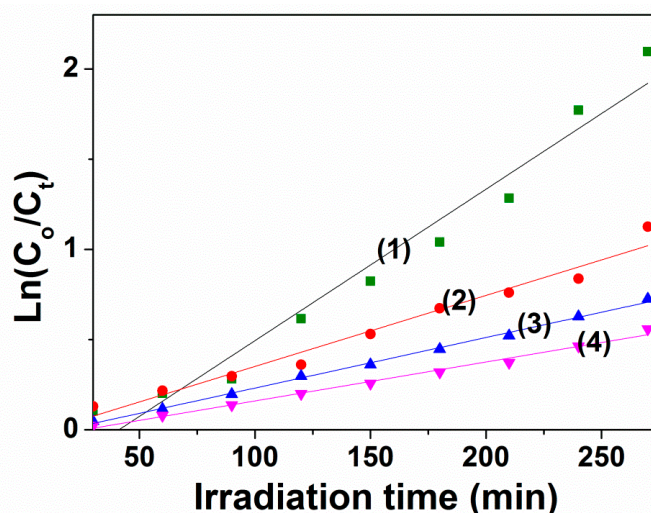
Figure 10. The plots of $\ln(C_o/C_t)$ versus irradiation time (t) in the presence of H_2O_2 and $CoFe_2O_4$ nanoparticles: (**1**) CF500, (**2**) CF600, (**3**) CF700, (**4**) CF800.

Table 3. Pseudo first order rate constant (k) for the photocatalytic degradation of RhB using $CoFe_2O_4$ nanoparticles.

Samples	Rate Constant, ($k \times 10^{-2}$ min^{-1})	R^2
CF500	0.839	0.960
CF600	0.394	0.967
CF700	0.280	0.997
CF800	0.216	0.990

4. Conclusions

$CoFe_2O_4$ spinel nanoparticles were successfully synthesized via solution combustion method using urea as a fuel. The effect of annealing temperature on phase composition, morphology, optical property, and magnetic properties of $CoFe_2O_4$ materials was studied. The crystallite size calculated by the Scherer formula increased from 9 to 29 nm with an increase in the annealing temperature. By elevating the annealing temperature, it was found that the band gap energy value and saturation magnetization of $CoFe_2O_4$ spinel were also accordingly increased. The photocatalytic degradation against RhB dye of $CoFe_2O_4$ spinel decreased with increasing annealed temperature. Among all the cobalt ferrite samples, CF500 exhibited an enhanced degradation efficiency of 90.6% at a visible light exposure time of 270 min. The first-order rate constant for CF500 was 0.839×10^{-2} min^{-1} and was 3.9 times faster than CF800. The photocatalytic degradation of RhB dye followed first order kinetics. The current results suggest a possible application of cobalt ferrites nanoparticles in treatment of dye-contaminated water.

Author Contributions: Investigation, N.T.H.L., N.T.T.H., N.Q.H., D.T.T.A., V.T.H., L.V.T. and T.V.T.; Writing—original draft, N.T.T.L.

Conflicts of Interest: The authors declare no conflict of interest.

References

1. Phong, P.T.; Phuc, N.X.; Nam, P.H.; Chien, N.V.; Dung, D.D.; Linh, P.H. Size-controlled heating ability of $CoFe_2O_4$ nanoparticles foráhyperthermia applications. *Phys. B Condens. Matter* **2018**, *531*, 30–34. [CrossRef]
2. Kumar, E.R.; Jayaprakash, R.; Kumar, S. Effect of annealing temperature on structural and magnetic properties of manganese substituted $NiFe_2O_4$ nanoparticles. *Mater. Sci. Semicond. Process.* **2014**, *17*, 173–177. [CrossRef]
3. Tong, J.; Bo, L.; Li, Z.; Lei, Z.; Xia, C. Magnetic $CoFe_2O_4$ nanocrystal: A novel and efficient heterogeneous catalyst for aerobic oxidation of cyclohexane. *J. Mol. Catal. A Chem.* **2009**, *307*, 58–63. [CrossRef]
4. Rao, K.S.; Choudary, G.; Rao, K.H.; Sujatha, C. Structural and magnetic properties of ultrafine $CoFe_2O_4$ nanoparticles. *Procedia Mater. Sci.* **2015**, *10*, 19–27. [CrossRef]
5. Kumar, S.; Munjal, S.; Khare, N. Metal-semiconductor transition and Seebeck inversion in $CoFe_2O_4$ nanoparticles. *J. Phys. Chem. Solids* **2017**, *105*, 86–89. [CrossRef]
6. Salazar-Kuri, U.; Estevez, J.O.; Silva-González, N.R.; Pal, U. Large magnetostriction in chemically fabricated $CoFe_2O_4$ nanoparticles and its temperature dependence. *J. Magn. Magn. Mater.* **2018**, *460*, 141–145. [CrossRef]
7. Annie Vinosha, P.; Jerome Das, S. Investigation on the role of pH for the structural, optical and magnetic properties of cobalt ferrite nanoparticles and its effect on the photo-fenton activity. *Mater. Today Proc.* **2018**, *5*, 8662–8671. [CrossRef]
8. Dong, N.; He, F.; Xin, J.; Wang, Q.; Lei, Z.; Su, B. Preparation of $CoFe_2O_4$ magnetic fiber nanomaterial via a template-assisted solvothermal method. *Mater. Lett.* **2015**, *141*, 238–241. [CrossRef]
9. Varma, P.C.R.; Manna, R.S.; Banerjee, D.; Varma, M.R.; Suresh, K.G.; Nigam, A.K. Magnetic properties of $CoFe_2O_4$ synthesized by solid state, citrate precursor and polymerized complex methods: A comparative study. *J. Alloys Compd.* **2008**, *453*, 298–303. [CrossRef]

10. Maleki, A.; Hosseini, N.; Taherizadeh, A. Synthesis and characterization of cobalt ferrite nanoparticles prepared by the glycine-nitrate process. *Ceram. Int.* **2018**, *44*, 8576–8581. [CrossRef]

11. Gabal, M.A.; Al-Juaid, A.A.; El-Rashed, S.; Hussein, M.A. Synthesis and characterization of nano-sized CoFe2O4 via facile methods: A comparative study. *Mater. Res. Bull.* **2017**, *89*, 68–78. [CrossRef]

12. Pourgolmohammad, B.; Masoudpanah, S.M.; Aboutalebi, M.R. Synthesis of $CoFe_2O_4$ powders with high surface area by solution combustion method: Effect of fuel content and cobalt precursor. *Ceram. Int.* **2017**, *43*, 3797–3803. [CrossRef]

13. Rajan Babu, D.; Venkatesan, K. Synthesis of nanophasic $CoFe_2O_4$ powder by self-igniting solution combustion method using mix up fuels. *J. Cryst. Growth* **2017**, *468*, 179–184. [CrossRef]

14. Yadav, N.G.; Chaudhary, L.S.; Sakhare, P.A.; Dongale, T.D.; Patil, P.S.; Sheikh, A.D. Impact of collected sunlight on $ZnFe_2O_4$ nanoparticles for photocatalytic application. *J. Colloid Interface Sci.* **2018**, *527*, 289–297. [CrossRef]

15. Kalam, A.; Al-Sehemi, A.G.; Assiri, M.; Du, G.; Ahmad, T.; Ahmad, I.; Pannipara, M. Modified solvothermal synthesis of cobalt ferrite ($CoFe_2O_4$) magnetic nanoparticles photocatalysts for degradation of methylene blue with H2O2/visible light. *Results Phys.* **2018**, *8*, 1046–1053. [CrossRef]

16. Vinosha, P.A.; Xavier, B.; Anceila, D.; Das, S.J. Nanocrystalline ferrite (MFe_2O_4, M = Ni, Cu, Mn and Sr) photocatalysts synthesized by homogeneous Co-precipitation technique. *Optik* **2018**, *157*, 441–448. [CrossRef]

17. Guo, X.; Wang, K.; Li, D.; Qin, J. Heterogeneous photo-Fenton processes using graphite carbon coating hollow $CuFe_2O_4$ spheres for the degradation of methylene blue. *Appl. Surf. Sci.* **2017**, *420*, 792–801. [CrossRef]

18. Kurian, M.; Nair, D.S. Heterogeneous Fenton behavior of nano nickel zinc ferrite catalysts in the degradation of 4-chlorophenol from water under neutral conditions. *J. Water Process Eng.* **2015**, *8*, e37–e49. [CrossRef]

19. Annie Vinosha, P.; Xavier, B.; Ashwini, A.; Ansel Mely, L.; Jerome Das, S. Tailoring the photo-Fenton activity of nickel ferrite nanoparticles synthesized by low-temperature coprecipitation technique. *Optik* **2017**, *137*, 244–253. [CrossRef]

20. Nguyen, L.T.T.; Nguyen, L.T.H.; Manh, N.C.; Quoc, D.N.; Quang, H.N.; Nguyen, H.T.T.; Nguyen, D.C.; Bach, L.G. A Facile Synthesis, Characterization, and Photocatalytic Activity of Magnesium Ferrite Nanoparticles via the Solution Combustion Method. *J. Chem.* **2019**, *2019*, 3428681. [CrossRef]

21. Xie, H.; Gu, S.; Zhang, J.; Hu, Q.; Yu, X.; Kong, J. Novel PEI–AuNPs–MnIIIPPIX nanocomposite with enhanced peroxidase-like catalytic activity in aqueous media. *C. R. Chim.* **2018**, *21*, 104–111. [CrossRef]

22. Sahnoun, S.; Boutahala, M.; Tiar, C.; Kahoul, A. Adsorption of tartrazine from an aqueous solution by octadecyltrimethylammonium bromide-modified bentonite: Kinetics and isotherm modeling. *C. R. Chim.* **2018**, *21*, 391–398. [CrossRef]

23. Khelifi, S.; Ayari, F. Modified bentonite for anionic dye removal from aqueous solutions. Adsorbent regeneration by the photo-Fenton process. *C. R. Chim.* **2019**, *22*, 154–160. [CrossRef]

24. da Rosa, A.L.D.; Carissimi, E.; Dotto, G.L.; Sander, H.; Feris, L.A. Biosorption of rhodamine B dye from dyeing stones effluents using the green microalgae Chlorella pyrenoidosa. *J. Clean. Prod.* **2018**, *198*, 1302–1310. [CrossRef]

25. Van Tran, T.; Nguyen, D.T.C.; Le, H.T.N.; Duong, C.D.; Bach, L.G.; Nguyen, H.-T.T.; Nguyen, T.D. Facile synthesis of manganese oxide-embedded mesoporous carbons and their adsorbability towards methylene blue. *Chemosphere* **2019**, *227*, 455–461. [CrossRef]

26. Sanchez-Hachair, A.; Hofmann, A. Hexavalent chromium quantification in solution: Comparing direct UV–visible spectrometry with 1,5-diphenylcarbazide colorimetry. *C. R. Chim.* **2018**, *21*, 890–896. [CrossRef]

27. Ignat, M.; Rotaru, R.; Samoila, P.; Sacarescu, L.; Timpu, D.; Harabagiu, V. Relationship between the component synthesis order of zinc ferrite–titania nanocomposites and their performances as visible light-driven photocatalysts for relevant organic pollutant degradation. *C. R. Chim.* **2018**, *21*, 263–269. [CrossRef]

28. Dimić, D. The importance of specific solvent–solute interactions for studying UV–vis spectra of light-responsive molecular switches. *C. R. Chim.* **2018**, *21*, 1001–1010. [CrossRef]

29. Sharma, R.; Singhal, S. Structural, magnetic and electrical properties of zinc doped nickel ferrite and their application in photo catalytic degradation of methylene blue. *Phys. B Condens. Matter* **2013**, *414*, 83–90. [CrossRef]

30. Van Tran, T.; Nguyen, D.T.C.; Le, H.T.N.; Bach, L.G.; Vo, D.-V.N.; Lim, K.T.; Nong, L.X.; Nguyen, T.D. Combined Minimum-Run Resolution IV and Central Composite Design for Optimized Removal of Tetracycline Drug Over Metal–Organic Framework-Templated Porous Carbon. *Molecules* **2019**, *24*, 1887. [CrossRef]

31. Jinisha, R.; Gandhimathi, R.; Ramesh, S.T.; Nidheesh, P.V.; Velmathi, S. Removal of rhodamine B dye from aqueous solution by electro-Fenton process using iron-doped mesoporous silica as a heterogeneous catalyst. *Chemosphere* **2018**, *200*, 446–454. [CrossRef] [PubMed]

32. Shi, P.; Hu, X.; Wang, Y.; Duan, M.; Fang, S.; Chen, W. A PEG-tannic acid decorated microfiltration membrane for the fast removal of Rhodamine B from water. *Sep. Purif. Technol.* **2018**, *207*, 443–450. [CrossRef]

33. Saleh, T.A.; Ali, I. Synthesis of polyamide grafted carbon microspheres for removal of rhodamine B dye and heavy metals. *J. Environ. Chem. Eng.* **2018**, *6*, 5361–5368. [CrossRef]

34. Tuzen, M.; Sarı, A.; Saleh, T.A. Response surface optimization, kinetic and thermodynamic studies for effective removal of rhodamine B by magnetic AC/CeO_2 nanocomposite. *J. Environ. Manag.* **2018**, *206*, 170–177. [CrossRef] [PubMed]

35. Guégan, R. Organoclay applications and limits in the environment. *C. R. Chim.* **2019**, *22*, 132–141. [CrossRef]

36. Nabbou, N.; Belhachemi, M.; Boumelik, M.; Merzougui, T.; Lahcene, D.; Harek, Y.; Zorpas, A.A.; Jeguirim, M. Removal of fluoride from groundwater using natural clay (kaolinite): Optimization of adsorption conditions. *C. R. Chim.* **2019**, *22*, 105–112. [CrossRef]

37. Abidi, N.; Duplay, J.; Jada, A.; Errais, E.; Ghazi, M.; Semhi, K.; Trabelsi-Ayadi, M. Removal of anionic dye from textile industries' effluents by using Tunisian clays as adsorbents. Zeta potential and streaming-induced potential measurements. *C. R. Chim.* **2019**, *22*, 113–125. [CrossRef]

38. Van Tran, T.; Nguyen, D.T.C.; Nguyen, H.-T.T.; Nanda, S.; Vo, D.-V.N.; Do, S.T.; Van Nguyen, T.; Thi, T.A.D.; Bach, L.G.; Nguyen, T.D. Application of Fe-based metal-organic framework and its pyrolysis products for sulfonamide treatment. *Environ. Sci. Pollut. Res.* **2019**, *26*, 28106–28126. [CrossRef]

39. Sundararajan, M.; John Kennedy, L.; Nithya, P.; Judith Vijaya, J.; Bououdina, M. Visible light driven photocatalytic degradation of rhodamine B using Mg doped cobalt ferrite spinel nanoparticles synthesized by microwave combustion method. *J. Phys. Chem. Solids* **2017**, *108*, 61–75. [CrossRef]

40. Nadumane, A.; Shetty, K.; Anantharaju, K.S.; Nagaswarupa, H.P.; Rangappa, D.; Vidya, Y.S.; Nagabhushana, H.; Prashantha, S.C. Sunlight photocatalytic performance of Mg-doped nickel ferrite synthesized by a green sol-gel route. *J. Sci. Adv. Mater. Devices* **2019**, *4*, 89–100. [CrossRef]

41. Almessiere, M.A.; Slimani, Y.; Güner, S.; Nawaz, M.; Baykal, A.; Aldakheel, F.; Akhtar, S.; Ercan, I.; Belenli, İ.; Ozçelik, B. Magnetic and structural characterization of Nb^{3+}-substituted $CoFe_2O_4$ nanoparticles. *Ceram. Int.* **2019**, *45*, 8222–8232. [CrossRef]

42. Sharma, R.; Bansal, S.; Singhal, S. Augmenting the catalytic activity of $CoFe_2O_4$ by substituting rare earth cations into the spinel structure. *RSC Adv.* **2016**, *6*, 71676–71691. [CrossRef]

43. Han, L.; Zhou, X.; Wan, L.; Deng, Y.; Zhan, S. Synthesis of $ZnFe_2O_4$ nanoplates by succinic acid-assisted hydrothermal route and their photocatalytic degradation of rhodamine B under visible light. *J. Environ. Chem. Eng.* **2014**, *2*, 123–130. [CrossRef]

44. Wu, X.; Wang, W.; Li, F.; Khaimanov, S.; Tsidaeva, N.; Lahoubi, M. PEG-assisted hydrothermal synthesis of $CoFe_2O_4$ nanoparticles with enhanced selective adsorption properties for different dyes. *Appl. Surf. Sci.* **2016**, *389*, 1003–1011. [CrossRef]

45. Van Tran, T.; Nguyen, D.T.C.; Le, H.T.N.; Nguyen, O.T.K.; Nguyen, V.H.; Nguyen, T.T.; Bach, L.G.; Nguyen, T.D. A hollow mesoporous carbon from metal-organic framework for robust adsorbability of ibuprofen drug in water. *R. Soc. Open Sci.* **2019**, *6*, 190058. [CrossRef]

46. Van Tran, T.; Nguyen, D.T.C.; Le, H.T.N.; Bach, L.G.; Vo, D.-V.N.; Hong, S.S.; Phan, T.-Q.T.; Nguyen, T.D. Tunable Synthesis of Mesoporous Carbons from Fe_3O (BDC) 3 for Chloramphenicol Antibiotic Remediation. *Nanomaterials* **2019**, *9*, 237. [CrossRef]